

Orientation distributions of vacuum-deposited organic emitters revealed by single-molecule microscopy

Francisco Tenopala-Carmona^{1,2,}, Dirk Hertel¹, Sabina Hillebrandt¹, Andreas Mischok¹, Arko Graf², Klaus Meerholz¹, Malte C. Gather^{1,2,*}*

1. Humboldt Centre for Nano- and Biophotonics and Institute of Physical Chemistry, Department of Chemistry, University of Cologne, Greinstr. 4-6, 50939 Köln, Germany.
2. Organic Semiconductor Centre, SUPA School of Physics and Astronomy, University of St Andrews, St Andrews, KY16 9SS, UK.

*Email: Malte.Gather@uni-koeln.de, F.TenopalaCarmona@uni-koeln.de

Abstract

The orientation of luminescent molecules in organic light-emitting diodes (OLEDs) strongly influences device performance. However, our understanding of the factors controlling emitter orientation is limited as current measurements only provide ensemble-averaged orientation values. Here, we use single-molecule imaging to measure the transition dipole orientation of individual molecules in a state-of-the-art thermally evaporated host and thereby obtain complete orientation distributions of the hyperfluorescence-terminal emitter C545T. We achieve this by realizing ultra-low doping concentrations (10^{-6} wt%) of C545T and minimising background levels to reliably measure the photoluminescence of the emitter. This approach yields the orientation distributions of >1000 individual emitter molecules in a system relevant to vacuum-processed OLEDs. Analysis of solution- and vacuum-processed systems reveals that the orientation distributions strongly depend on the nanoscale environment of the emitter. This work opens the door to attaining unprecedented information on the factors that determine emitter orientation in current and future material systems for OLEDs.

Introduction

Organic light-emitting diodes (OLEDs) are an important class of organic semiconductor devices that provide versatile, efficient emission in a wide range of applications. Improving device efficiency and stability by maximising the extraction of light from OLEDs is one of the main research priorities in this field.^{1,2} Horizontal alignment of the transition dipole moment (TDM) of emitter molecules is a popular and impactful strategy to achieve this without needing to add a dedicated outcoupling structure, which can increase processing costs.^{3–6} Instead, this strategy relies on making use of the anisotropic distribution of the dipole radiation from molecules that align during their deposition.

The emissive layers of efficient OLEDs are commonly fabricated by either thermally evaporating the molecules under high vacuum or depositing them from solution via spin-coating or printing.^{7,8} Several important factors that appear to promote horizontal TDM alignment in vacuum-processed emitters have been identified,^{3–9} and the alignment of small-molecule emitters in solution-processed layers for OLEDs is also receiving increasing attention.^{10,11} However, many factors relevant to both processing methods—such as dipolar interactions, hydrogen bonding, host alignment, and the influence of the underlying layers—have only recently started to be examined systematically or remain unexplored.^{3,4,12–14} In most state-of-the-art devices, small emitter molecules that efficiently convert electronic excitation into light are doped into host molecules to avoid the detrimental effects that frequently arise when two excited molecules are in close proximity.^{15,16} Therefore, host-emitter interactions during film formation are particularly relevant to the orientation of emitters in doped films.^{3–6,12,14}

Our understanding of TDM alignment in these systems is limited by the amount of information we can obtain using current measurement techniques. Most molecular-orientation studies rely on angle-resolved photoluminescence spectroscopy (ARPL)—or related angle-resolved luminescence spectroscopy techniques—and variable-angle spectroscopic ellipsometry (VASE).^{3–5} These methods can determine the average orientation of the TDM of the emission or absorption of molecules, e.g., in terms of the anisotropy factor $a \equiv \langle \cos^2 \theta \rangle$, where θ is the angle between the TDM and the normal to the film, or through other related parameters.^{3,4,6} Thereby, the orientation of emitters in OLEDs is commonly classified in relation to three limiting cases; namely, perfectly horizontal ($a = 0$), isotropic ($a = 1/3$), or perfectly vertical ($a = 1$) orientations. Crucially, by definition, currently used orientation parameters always average the orientation of the emitter molecules in the film over the entire ensemble and only give the first moment of their orientation distribution. Therefore, two

ensembles of molecules that differ in width, peak value, skewness, or shape can have the same anisotropy factor (**Fig. 1a, Supplementary Fig. 1**). Measurement of the orientation distributions could provide valuable insight into the factors that drive molecular orientation, but this is currently not possible experimentally. Computational methods can model intermolecular interactions during film formation, which can in turn yield predictions of the orientation of molecules in thin films.^{4,17–22} However, these models can only consider a limited number of atoms, and experimental validations beyond ensemble-averaged measurements remain elusive. Therefore, the ability to experimentally obtain the orientation distributions of emitters could provide significantly more information on the range of host-emitter interactions that drive molecular alignment in OLED-relevant systems.

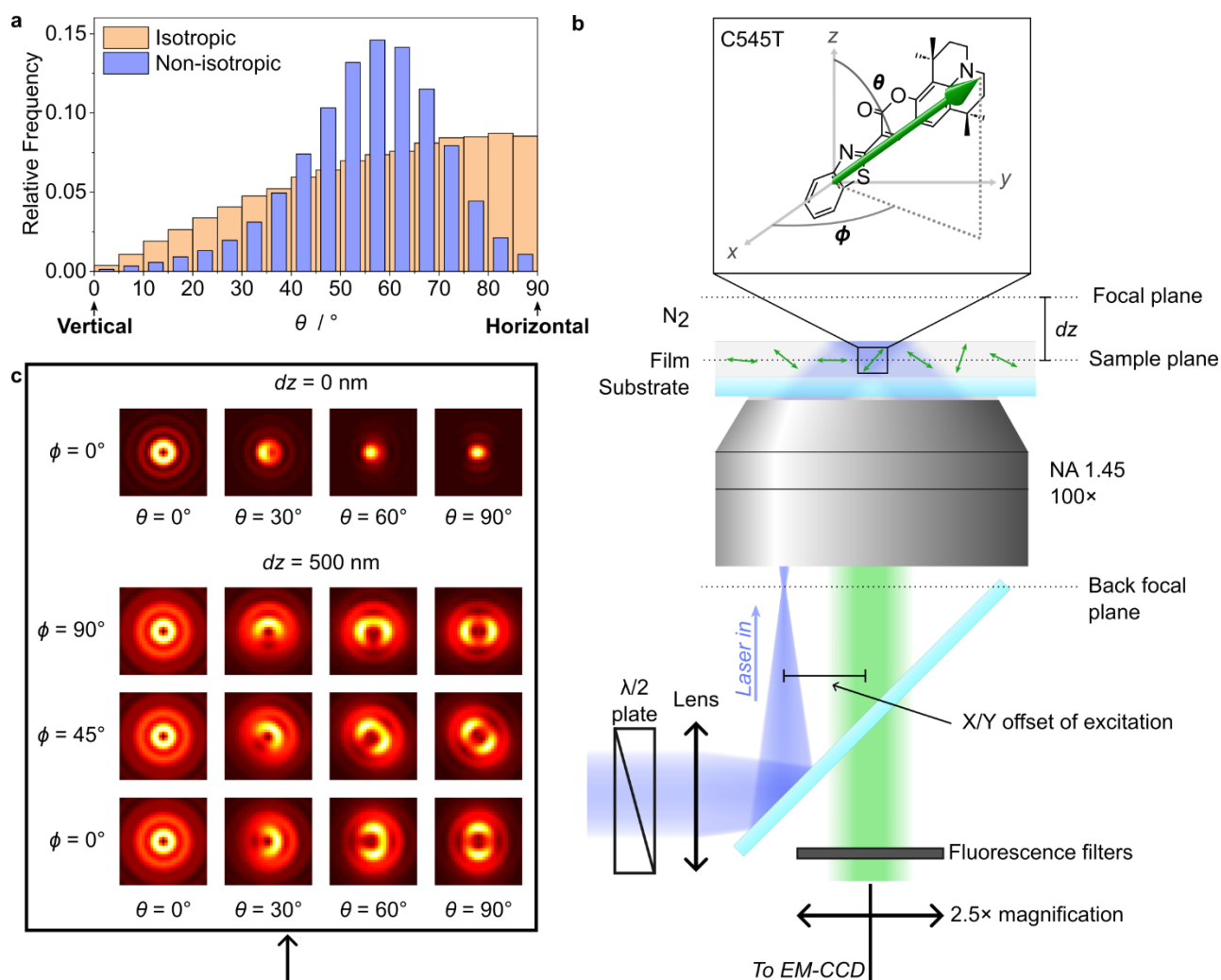


Figure 1: Measurement of the orientation of single molecules via single-molecule defocused orientation and position imaging (DOPI). **a**, Illustrative comparison of an isotropic orientation distribution (proportional to $\sin \theta$) and a hypothetical non-isotropic distribution with a maximum at $\sim 57^\circ$ and a narrow width. The anisotropy factor is the same for both distributions ($a = 0.33$). The data for these hypothetical examples were obtained using a

random-number generator (see **Supplementary Section 1**). **b**, Schematic of the microscope setup for single-molecule DOPI. A linearly polarized blue laser beam is focused to the back focal plane of a high-NA objective with a variable X/Y offset from the optical axis. This results in wide-field, variable-angle excitation of a film containing dispersed emitter molecules. The film is placed at $dz \sim 500$ nm away from the focal plane of the objective to create intentionally defocused images of the photoluminescence of individual emitter molecules on the EM-CCD camera. The inset shows the chemical structure of the hyperfluorescence-terminal emitter C545T and the direction of its $S_1 \rightarrow S_0$ transition dipole moment (TDM). Data taken from Ref. ²³. **c**, Optical simulations of in-focus (top) and out-of-focus (bottom) single-molecule orientation patterns.

Here, we adapt and develop DOPI to measure the complete orientation distribution of the TDM of emitter molecules in state-of-the-art vacuum-deposited OLEDs. To achieve this, we thermally evaporate organic emitters at low enough rates to measure the photoluminescence from individual molecules. Furthermore, we eliminate the excitation bias commonly present in SMFM via a complementary-polarisation excitation scheme. Finally, we show that by optimized, thorough purification of a state-of-the-art OLED host material and careful management of the excitation and imaging conditions, we can attain sufficient signal-to-noise and signal-to-background ratios to experimentally measure the orientation distribution of thousands of single molecules of the hyperfluorescence-terminal emitter Coumarin 545T (C545T).⁴¹ Comparisons of measurements in inert solution-processed polymer matrices and OLED-relevant vacuum-deposited systems reveal that the orientation distribution of the emitter molecules in a doped film strongly depends on the processing conditions, and that the shape of the distributions can differ significantly—even for distributions with similar anisotropy factors. Moreover, we observe substantial differences in the orientation distribution of emitters located in different planes within the same film, which is particularly relevant for studying how the nano-scale morphology of films influences emitter orientation. These findings demonstrate how our technique can expand the current understanding of the factors that drive emitter orientation in OLEDs by providing an experimental means to link molecular-scale interactions to macroscopic device properties.

Results

Minimising excitation bias in defocused imaging of single emitter molecules

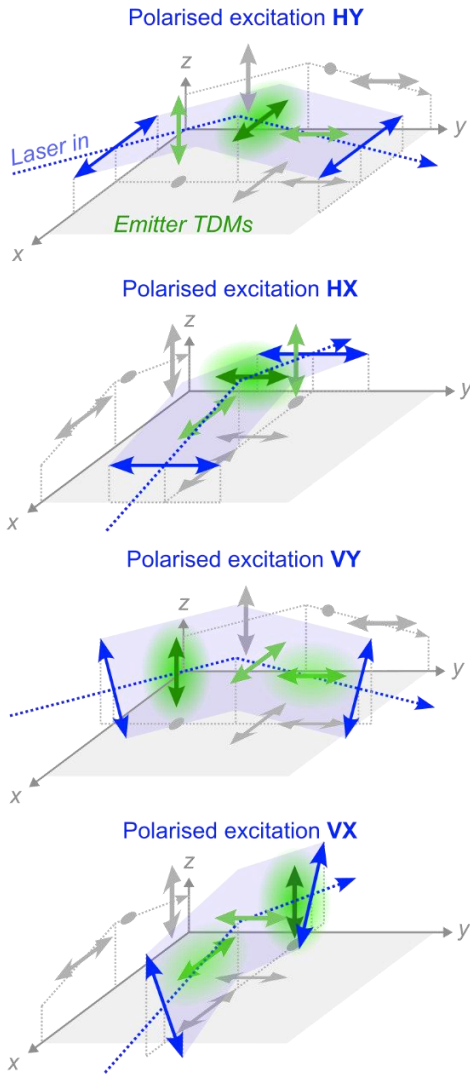
Figure 1b illustrates the general strategy employed to measure the orientation of individual molecules. The photoluminescence of spatially separated molecules in a thin film is imaged with the film positioned ~ 500 nm out of the focal plane of the microscope objective. The

resulting diffraction patterns observed on the camera are specific to the polar and azimuthal orientation of the TDM of each molecule (**Fig. 1c**). The polar and azimuthal angles of the TDM relative to the plane of the film (ϕ , θ), as well as the three-dimensional position of the molecule in the film (x , y , z), can be determined by comparing and fitting the measured patterns to optical simulations via a least-square error minimisation algorithm (see **Methods** and **Supplementary Section 2** for details of experimental conditions and data analysis).

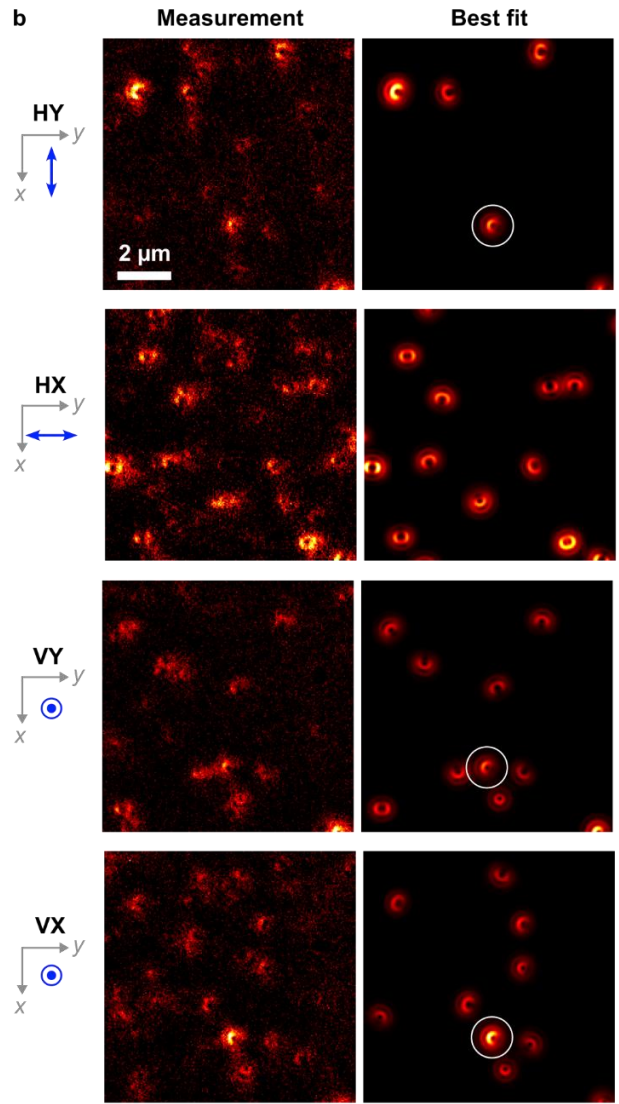
For initial tests and referencing, we spin-coated thin films containing C545T doped at $\sim 10^{-6}$ wt% into the transparent polymer poly(methyl methacrylate) (PMMA, **Supplementary Fig. 3**). These samples were first imaged in-focus to determine the optimum concentration for orientation measurements (**Supplementary Fig. 4**). The number of emissive molecules per field of view ($40 \times 40 \mu\text{m}^2$) increased linearly with the concentration of C545T in the spin-coated solution, demonstrating that single molecules are resolvable and isolated from each other.

Next, single-molecule orientation patterns were imaged out of focus. Köhler illumination is usually used in epifluorescence excitation, i.e., the excitation beam travels along the normal to the sample plane, which can lead to sampling biases of an ensemble of fluorescent molecules because the electric field oscillates parallel to the horizontal plane. This issue was previously addressed by splitting the excitation beam using custom-built prism arrays;⁴² this configuration allows the sample to be illuminated by two beams providing simultaneous in- and out-of-plane excitation. While useful for measuring dynamic processes in single molecules,⁴³ this arrangement can lead to interference effects between the beams.⁴² The static nature of our sample and the high photostability of OLED emitter materials allowed us instead to sequentially excite the sample along the three orthogonal directions by displacing and focusing the excitation beam close to the edge of the back focal plane aperture of the objective (**Fig. 1b**). This strategy results in different wide-field excitation configurations, each with linear polarisation approximately along one of the three orthogonal axes of the sample which, in turn, depend on the linear polarisation and propagation direction of the beam (**Fig. 2a**). Each configuration excites a different subset of emitter molecules in a given field of view (**Fig. 2b**). Consequently, the measured distribution of the polar and azimuthal orientation angles strongly depends on the polarisation of the excitation beam (**Supplementary Fig. 5**). In order to avoid double-counting molecules in different excitation conditions, molecules that coincided in position and orientation angles across different measurements are identified and discarded (**Fig. 2b**) before all datasets are incorporated into a final set.

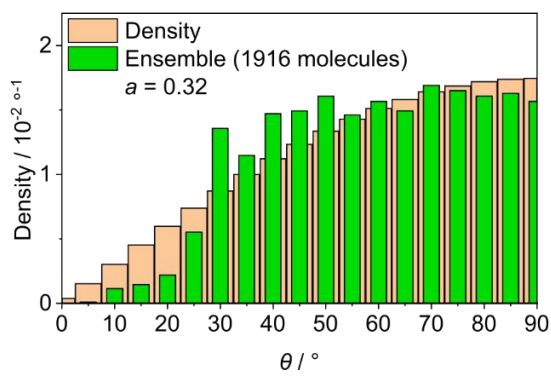
a



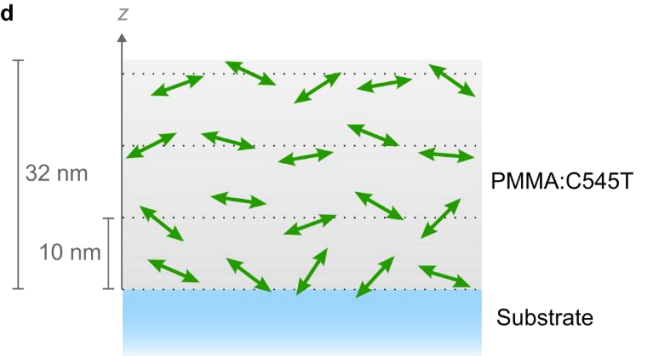
b



c



d



e

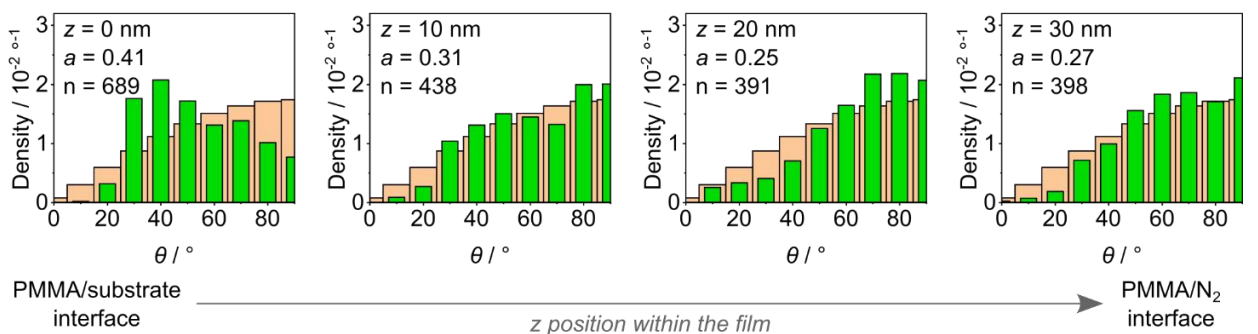


Figure 2. Orientation distributions of C545T in PMMA. **a**, Illustration of the complementary-polarisation excitation conditions used for DOPI. Each configuration is characterized by the linear polarisation state of the excitation beam, which is parallel or perpendicular to the plane of the films (labelled H and V, respectively), and its direction of propagation along the XZ or YZ planes (labelled X and Y, respectively). **b**, Examples of DOPI patterns measured with the excitation condition shown to the left of each panel. All measurements shown are for the same field of view. The best-fit optical simulations are shown for comparison. The patterns strongly depend on the polarisation of the laser beam. A representative pattern seen under HY, VX, and VY excitation is marked by a white circle. **c**, Orientation distribution of polar angles for all detected C545T emitters. The distribution approaches the isotropic limit for large angles, but clearly deviates at smaller angles. **d**, Schematic of a spin-coated film composed of C545T molecules dispersed in the transparent host PMMA. Horizontal dotted lines mark the different z positions used for optical simulations. **e**, Histogram of polar angles for emitters at different vertical positions (z) within the film. The orientation distributions are different for each z value; this is also reflected in different anisotropy factors for each sub-ensemble.

A histogram of the polar angles of C545T molecules in PMMA obtained in this manner exhibits a broad distribution that falls abruptly for $\theta < 30^\circ$ (**Fig. 2c**). The mean a value obtained directly from computing $\langle \cos^2\theta \rangle$ of this dataset is 0.32, which is close to the value seen for an isotropic distribution. ARPL measurements of a reference sample (1 wt% C545T in PMMA) were in good agreement with those obtained from the single-molecule distribution ($a = 0.33$, **Supplementary Fig. 6**). However, the distribution obtained from our DOPI measurements differs from an isotropic distribution. This is more clearly visible for θ between 30° and 50° , where the distribution is higher than the isotropic limit, and towards 0° (vertical axis), where the frequency counts fall below it. This deviation from the isotropic case is likely due to interactions between the polymer host, the emitter molecules, and the substrate during film formation (see below). We emphasise that the complementary-polarisation excitation eliminates any bias towards exciting horizontally oriented molecules.

Orientation distributions at different heights across a film

The defocused orientation patterns are sensitive to the vertical position of the individual molecules within the film (**Supplementary Fig. 7**). This allowed us to obtain orientation distributions for the TDMs of molecules at four different positions: near the interface to the glass substrate ($z = 0$ nm), 10 nm and 20 nm away from the substrate, and close to the top surface of the film ($z = 30$ nm) (**Fig. 2d**). Different peaks are distinguishable at each z -position (**Fig. 2e**): a narrow peak at 40° dominates the orientation distribution of molecules near the

glass substrate, followed by a second peak at 70° . The distribution shifts towards larger angles for $z = 10$ nm, with a main peak at 80° and second peak still visible at 50° . The distribution shifts even further to horizontal orientations at $z = 20$ nm, where the peak remains at 80° and no other peaks are resolvable. Finally, the distribution shifts slightly back to smaller angles at $z = 30$ nm, even though the maximum is at 90° . From these distributions, we can also compute anisotropy factors for each position. The anisotropy factor is highest near the glass substrate ($a = 0.41$), reflecting the preferentially vertical orientation of the emitter TDMs ($a > 1/3$). As z increases, a reaches a minimum at $z = 20$ nm ($a = 0.25$, preferentially horizontal orientation) and shifts back to a less horizontal value near the top surface of the film ($a = 0.27$).

Based on these changes in orientation distribution across the height of the PMMA film, we hypothesise that the tendency of emitter TDMs to align horizontally within the film and near its top surface is a consequence of the centrifugal force during the spin-coating process, the intrinsic geometric anisotropy of the PMMA host and, potentially, that of the C545T emitters; as solvent molecules evaporate, preferentially horizontal polymer chains trap emitter molecules within the film. By contrast, the preferentially vertical orientation of the emitters near the glass substrate is likely a result of the interaction of PMMA and C545T with the substrate surface, presumably due to either friction or poor solvation at the boundary.⁴⁴

To summarize, the orientation of C545T molecules in PMMA is not isotropic across the film, even though the anisotropy factor measured for the ensemble case is close to that of the isotropic case. Furthermore, the orientation distribution depends on the vertical position of the emitters within the film. It is commonly assumed that small molecules adopt an isotropic orientation during the spin-coating process, but our single molecule-resolved data show that this is not the case here.

Single-molecule orientation distributions of emitters in OLED-relevant systems

Single-molecule imaging requires careful control over the number of target molecules in the field of view, as well as the numbers of fluorescent impurities that may compete with photoluminescence from the target molecules. To meet these requirements for vacuum-deposited films, evaporation rates far below the detection threshold of quartz crystal microbalance (QCM) sensors in commercial systems are needed, and photoluminescent impurities in both the deposition chamber and the host materials must be meticulously managed.

First, we deposited low-enough concentrations of C545T molecules on bare glass substrates by significantly decreasing the temperature of the evaporation crucible and carefully adjusting the duration of time that the substrates are exposed to incoming emitter molecules. For C545T, a crucible temperature of 313 K yielded a low-enough evaporation rate to enable control of the emitter concentration on the substrate by varying the deposition time with adjustable shutters (see **Methods** for further details). Depositions lasting a few minutes were sufficient to reliably disperse single emitter molecules on the substrate surface with enough separation to perform DOPI, i.e., ~500 molecules in a $40 \times 40 \mu\text{m}^2$ field of view (**Fig. 3a,b**). Importantly, no molecules were detected on substrates exposed to an empty crucible heated to 313 K for similar durations or when the substrate was exposed while the filled crucible was not actively heated (**Supplementary Fig. 8**), which confirmed that the measured molecules are the target C545T emitter.

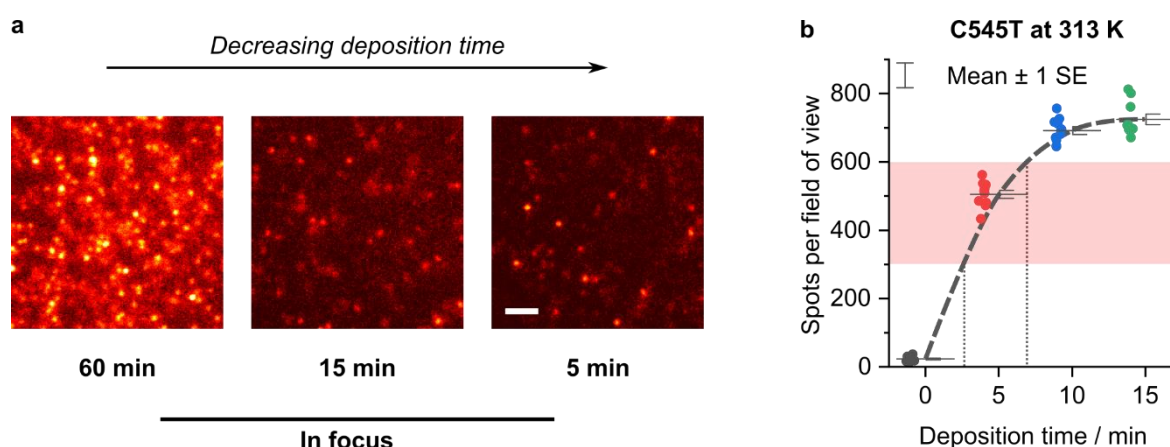


Figure 3. Thermal evaporation of C545T molecules at concentrations suitable for SMFM. **a**, In-focus single molecule fluorescence images of vacuum-deposited C545T on glass substrates. Spots overlap for deposition times of 15 min and longer, but diffraction-limited spots from single molecule emission are resolvable when the deposition time is reduced to 5 min. Scale bar, $2 \mu\text{m}$. **b**, Number of emissive spots per field of view ($\sim 40 \times 40 \mu\text{m}^2$) as a function of C545T deposition time. The number of resolvable spots saturates at long times, as emission from neighbouring molecules begins to overlap. The red shaded area indicates the target concentration range. The grey dashed line is shown as a guide to the eye. A deposition time of 0 min corresponds to substrates that were placed inside the chamber but remained covered during the whole process using the adjustable shutters.

In addition, we found that it is crucial to minimise the exposure of the substrates to fluorescent impurities from the evaporation chamber. Significant numbers of fluorescent molecules were found on substrates left in the evaporation chamber under high vacuum for long periods of time (> 3 hours), even when no C545T was placed in the crucible

(Supplementary Fig. 8). Presumably, this contamination results from desorption of fluorescent molecules from the walls or other parts of the evaporation chamber. Shielding the substrates at all times, except during the deposition process, effectively prevented contamination of the substrate with non-target molecules.

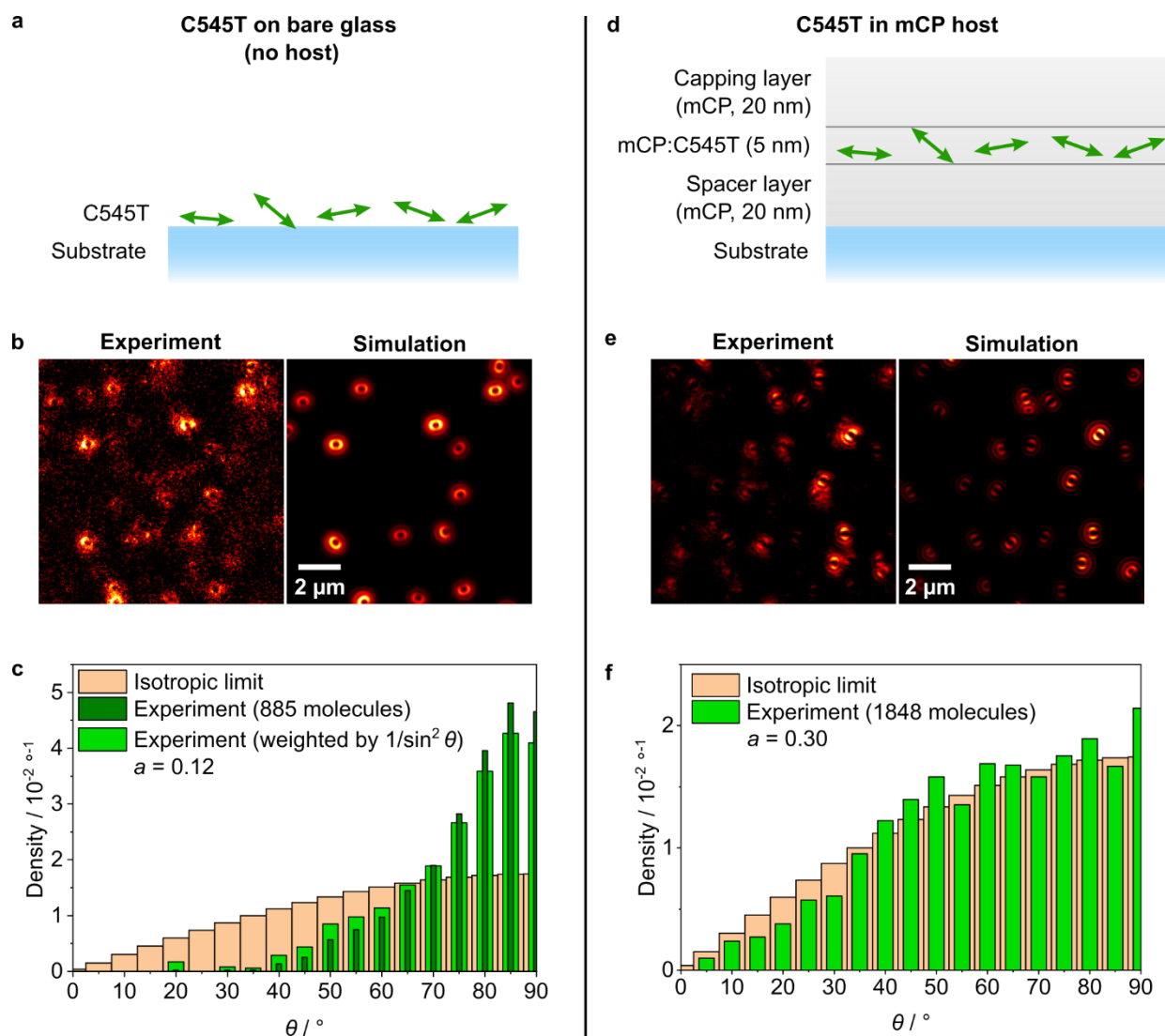


Figure 4. Orientation distributions of C545T in vacuum-processed systems. **a**, Illustration of TDMs of individual C545T molecules adsorbed on a glass substrate. **b**, Defocused orientation patterns measured with in-plane excitation with circularly polarised light. The best-fit optical simulations are shown for comparison. **c**, Distribution of polar angles of the TDMs of C545T emitters on glass, as measured (dark green) and after dividing by $\sin^2 \theta$ (with an artificial zero at $\theta = 0^\circ$) to account for the excitation bias from the excitation configuration used in this measurement (light green). **d**, Illustration of the TDMs of individual C545T molecules dispersed in an mCP film, as fabricated in our experiments. **e**, Representative defocused orientation patterns of C545T molecules in mCP using excitation configuration HY (see Fig. 2a). The best-fit optical simulations are shown for comparison. **f**, Distribution of the polar angles of the TDMs of C545T emitters in mCP.

With a process for vacuum deposition of individual C545T molecules onto bare glass substrates established, we next measured the orientation distribution for these samples (**Fig. 4a**). Compared to C545T in PMMA, the molecules exhibited a significantly decreased brightness and photostability on bare glass, which led to a substantially reduced SNR of the defocused images (**Fig. 4b**). Given that all samples were encapsulated under nitrogen, we discard oxygen-driven photobleaching. Instead, we attribute this effect to charges on the surface of the glass substrate, presumably a residual from the cleaning process (see **Methods**). Charged species can induce reversible quenching of the luminescence from individual molecules (blinking),⁴⁵ as well as irreversible photodegradation (photobleaching).⁴⁶ We were still able to perform DOPI of these samples; however, only when using in-plane excitation with circularly polarised light. As expected for a relatively flat molecule like C545T,^{3,23} the resulting distribution of polar angles showed preferentially horizontal alignment of the TDMs of C545T molecules ($a = 0.12$), even after weighing the distribution with the different excitation probabilities inherent to in-plane excitation (**Fig. 4c**). The presence of orientation angles that deviate from purely horizontal may be a consequence of substrate roughness.

Next, we investigated the orientation distribution of C545T when co-deposited with the common OLED host 1,3-bis(N-carbazolyl)benzene (mCP; **Supplementary Fig. 3**). We sequentially deposited a 20 nm-thick spacer layer of pure mCP, a central 5 nm-thick co-deposited emissive layer, and a final 20 nm-thick capping layer of pure mCP (**Fig. 4d**). The spacer and capping layers ensure that the orientation of the emitter molecules is only driven by their interaction with the host, i.e., to minimise influence of the substrate on the orientation of the emitter,⁴⁷ and to enable host molecules in the capping layer to interact with buried emitter molecules, which might otherwise continue to diffuse on the surface of the film.

mCP shows very low absorption at the laser wavelength used for excitation (445 nm, **Supplementary Fig. 9**). To avoid background signal from any fluorescent impurities in the host material, we extensively purified mCP by three-fold vacuum sublimation. Combined with the high photostability and brightness of C545T, this provided a good SNR in the defocused patterns (**Fig. 4e**) and thus enabled reliable measurements of the TDM orientation distributions of C545T in mCP using our four configurations of complementary-polarisation excitation. The distribution of polar angles follows the isotropic limit more closely than in solution-processed PMMA films, albeit not exactly (**Fig. 4f**). The anisotropy factor computed from this distribution ($a = 0.31$), agrees well with ARPL measurements of the same emitter doped at 2 wt% in the same host ($a = 0.30$, **Supplementary Fig. 10**).

The near-isotropic distribution of C545T molecules is likely due to the relatively low molecular weight of C545T (430.5 g/mol) and the low glass transition temperature of mCP ($T_g \sim 338$ K).⁴⁸ Due to increased surface diffusion during deposition, small molecules are known to adopt orientations close to the isotropic limit when doped into materials with a low T_g , at least when considering the ensemble average of the orientation distribution.^{3,7,8,48} Our measurements now confirm that the orientation is indeed randomised at the level of individual molecules.

Discussion

By measuring the TDM orientation of individual molecules, we obtained complete orientation distributions of an OLED emitter material under a range of different conditions, including in a system relevant to vacuum-deposited hyperfluorescent OLEDs. To facilitate these measurements, we first established an excitation configuration that eliminates excitation bias. We then identified specific thermal evaporation conditions to deposit emitter molecules onto the substrate with sufficient separation to perform single-molecule DOPI. Combined with the use of a high-purity host, this approach enabled measurement of the TDM orientation of thousands of individual molecules in a high-throughput fashion. We also demonstrated the capability of this technique to unravel the different TDM orientation distributions of solution-processed samples with anisotropy factors close to the isotropic limit. Remarkably, the orientation distribution of C545T in PMMA varied significantly at different vertical positions within the same film, which highlights the importance of accounting for possible inhomogeneities in TDM orientation in future orientation studies of both solution-processed and vacuum-deposited OLEDs.

The findings of this initial study illustrate how our technique will provide unprecedented insight into the factors that drive emitter orientation in OLEDs, particularly the various preferred orientations of a single emitter in different hosts, as well as at different positions within the same host layer. These results underline the importance of orientation distributions in our understanding of the factors that drive emitter orientation in OLEDs. While widely used measurement techniques such as VASE and ARPL provide accurate average values, emitter orientation cannot be reduced to these averages from a materials science perspective.

SMFM measurements are limited by the brightness and photostability of the emitter that is studied. Therefore, these measurements require molecules with relatively high radiative

rates, which makes it challenging to apply our technique to phosphorescent compounds. However, fluorescent and state-of-the-art TADF emitters are good candidates for further studies that use DOPI to map the complete orientation distribution of an emitter.

In the future, the combination of DOPI measurements of vacuum-processed samples with quantum-chemical calculations of the same systems (e.g., molecular dynamics or Monte Carlo simulations) might contribute significantly to our understanding of how these preferred orientations occur and shed light on the importance of different intermolecular interactions for the orientation of OLED emitters. Moreover, the control achieved over the fabrication of vacuum-deposited samples and the spatial resolution provided by DOPI will help to address open questions such as the influence of interfaces—between the substrate and organic molecules, and also between different layers within an OLED—and the degree of order of the host on the orientation of emitter molecules.

Methods

Materials

C545T was obtained from Lumtec and used without further purification. mCP was obtained from Sigma Aldrich and purified in-house via three-fold vacuum sublimation using a Creaphys DSU05. PMMA was obtained from Sigma Aldrich and purified by three subsequent cycles of dilution in toluene and precipitation in isopropanol. KOH, acetone, isopropanol, methanol, and toluene were obtained from Fisher Scientific; all solvents were HPLC-grade or higher.

Substrate cleaning

For SMFM, borosilicate glass substrates (No. 1.5) were cleaned using the following cycle: 15 min ultrasonication in acetone, 15 min ultrasonication in methanol, rinse with milli-Q water, 5 min ultrasonication in milli-Q water, 15 min ultrasonication in 1 M KOH in milli-Q water, rinse twice with milli-Q water, 5 min ultrasonication in isopropanol (twice), drying under nitrogen flow, and 10 min treatment in an oxygen plasma system (for solution-processed samples) or in a UV-ozone cleaner (for vacuum-processed samples). Samples were prepared shortly after substrate cleaning to avoid contamination. For ARPL measurements, EagleXG glass substrates were cleaned by 15 min ultrasonication in acetone, 15 min ultrasonication in isopropanol, and finally 3 min oxygen-plasma treatment. For VASE measurements, silicon substrates with a native silicon oxide layer were cleaned in the same way as the glass substrates for ARPL, but the oxygen-plasma treatment was omitted to avoid thickening of the silicon oxide layer.

Fabrication of solution-processed samples for SMFM

C545T was diluted to ~5 nM in toluene via serial dilutions. For concentrations diluted to 100 nM or lower, only glassware (vials and pipettes) cleaned in the same way as the substrates were allowed to come into contact with the solutions. PMMA was diluted to ~30 mg/mL. Final dilutions of PMMA at ~10 mg/mL plus C545T at 0, ~100, ..., and ~500 pM were prepared in toluene and gently shaken for 15 min, then spin-coated at 2000 RPM for 30 s. Finally, the films were annealed at 100 °C for 10 min inside a nitrogen-filled glovebox to evaporate residual solvent, encapsulated with a cavity glass lid, and stored under nitrogen until the SMFM measurements were performed.

Fabrication of vacuum-processed samples for SMFM

Thermal evaporation was carried out in a commercial high-vacuum deposition system (Angstrom EvoVac) equipped with actively temperature-controlled furnaces for evaporation of organic materials (Luxel Radak I). Once placed inside the vacuum chamber, the substrates were protected by adjustable shutters placed ~2 mm away from their surface at all times, other than during the deposition step. All depositions were carried out at chamber pressures $< 5 \cdot 10^{-7}$ Torr. The deposition rate of C545T was controlled by keeping the crucible in the furnace at a pre-determined constant temperature. The deposition rate of the mCP host was set to 0.3 Å/s and controlled through a PID feedback loop using deposition rate readings from QCM sensors. All samples were encapsulated with a cavity glass lid inside a nitrogen-filled glove box without exposure to ambient conditions. All measurements were conducted shortly after fabrication to avoid recrystallisation of the host.

Fabrication of samples for ARPL

For solution-processed samples, a toluene solution of PMMA (~10 mg/mL) and C545T (~0.1 mg/mL) was spin-coated onto either EagleXG glass or silicon substrates at 2000 RPM for 30 s. The films were annealed at 100 °C for 10 min inside a nitrogen-filled glovebox to evaporate residual solvent. Films for ARPL were encapsulated with a cavity glass lid under nitrogen, and all samples were stored under nitrogen until measured.

For vacuum-deposited samples, 40 nm-thick films of C545T doped at 2 wt% in mCP were deposited at 0.6 Å/s on EagleXG glass substrates and on silicon substrates using the thermal-evaporation system described above. Films on glass substrates were immediately encapsulated with a cavity glass lid in a nitrogen-filled glove box. All samples were measured within 24 h to avoid recrystallisation of the host material.

Film characterisation via VASE

The thickness and optical constants of neat PMMA and mCP films, as well as of the films for ARPL measurements, were quantified via VASE (J.A. Woollam M2000 and subsequent modelling in software CompleteEASE). These data (**Supplementary Figs 10 and 11**) were used for analysis of the DOPI and ARPL data.

Single-molecule fluorescence microscopy

SMFM measurements were carried out on a Nikon Eclipse Ti-2 microscope equipped with a Perfect Focus System. Samples were excited with a Vortran Stardus CW laser (445 nm). The linear polarisation of the beam was controlled using a half-wave plate. The beam shape was cleaned and expanded using a telescope array and pinhole and cropped by a movable iris to produce an off-axis beam focused on the back-focal plane of an Olympus oil-immersion objective (NA 1.45, 100×). The power density of the laser at the sample plane was $\sim 36 \text{ W/cm}^2$. The light collected by the objective was passed through a dichroic (Semrock Di02-R442-25x36), and then through two further fluorescence filters (Semrock FF01-540/50-25 and Thorlabs FBH520-10) to discard fluorescence from non-target molecules. Finally, the image was expanded by a further 2.5× magnification and recorded using a Peltier-cooled EMCCD (Andor iXon Ultra 888), giving a field of view of $\sim 40 \times 40 \mu\text{m}^2$. The samples were first imaged in focus to quantify the number of molecules per field of view. Then, selected samples were imaged out-of-focus by displacing the objective to a fixed distance from the substrate using the Perfect Focus System.

Image processing

All image-processing and optical simulations were performed using MATLAB software (The MathWorks, Inc.). In-focus images to quantify the number of spots per field of view were processed using peak-finding and drift-correction algorithms obtained from the single-molecule image analysis package iSMS.⁴⁹ Optical simulations were obtained from the QDControl package from Enderlein et al.^{26,50} The pattern-matching algorithm of our analysis of defocused images followed the process reported by Patra et al.,²⁷ but was modified by addition of a segmentation algorithm to decrease the number of false positives. Additional algorithms for identifying double counts between different excitation configurations were developed in house. The complete image processing workflow is available at <DOI to be assigned upon acceptance>.

Angle-resolved photoluminescence spectroscopy measurements

ARPL of films deposited on EagleXG glass substrates was performed using a previously described custom-built setup.⁵¹ The data was fitted to optical simulations using the anisotropy factor of the average transition dipole of the emitters and the film thickness as free parameters.⁵²

Acknowledgements

The authors are grateful to Prof. J. Carlos Penedo for his advice and technical support on single-molecule microscopy and for providing the related laboratory facilities at the early stages of this project. This work was supported by the Volkswagen Foundation (No. 93404) and the DFG-funded Research Training Group “Template-Designed Organic Electronics (TIDE)”, RTG2591. M.C.G. acknowledges support from the Alexander von Humboldt Stiftung through the Humboldt-Professorship. A.M. acknowledges funding from the European Union’s Horizon 2020 research and innovation programme under Marie Skłodowska-Curie grant agreement No. 101023743 (PolDev).

Author Contributions

F.T.C. and M.C.G. designed the study and planned the experiments. F.T.C. fabricated the solution-processed samples, performed the SMFM measurements, wrote the custom-built SMFM data-processing algorithms, and performed ARPL measurements of the reference samples. D.H. purified the host material for vacuum-processed samples. S.H. and F.T.C. designed and fabricated the thermally evaporated samples. A.M. and F.T.C. performed the ellipsometry measurements and related analysis. A.G. performed preliminary SMFM studies of solution-processed samples and assisted in the analysis of DOPI data. All authors analysed and interpreted the results. F.T.C. and M.C.G. wrote the manuscript with contributions from all authors.

Competing interests

The authors declare no competing interests.

References

1. Gather, M. C. & Reineke, S. Recent advances in light outcoupling from white organic light-emitting diodes. *J Photonics Energy* **5**, 057607 (2015).
2. Salehi, A., Fu, X., Shin, D.-H. & So, F. Recent Advances in OLED Optical Design. *Adv Funct Mater* **29**, 1808803 (2019).
3. Tenopala-Carmona, F. *et al.* Identification of the Key Parameters for Horizontal Transition Dipole Orientation in Fluorescent and TADF Organic Light-Emitting Diodes. *Advanced Materials* **33**, 2100677 (2021).
4. Hofmann, A., Schmid, M. & Brütting, W. The Many Facets of Molecular Orientation in Organic Optoelectronics. *Adv Opt Mater* **9**, 2101004 (2021).
5. Kim, K.-H. & Kim, J.-J. Origin and Control of Orientation of Phosphorescent and TADF Dyes for High-Efficiency OLEDs. *Advanced Materials* **30**, 1705600 (2018).
6. Schmidt, T. D. *et al.* Emitter Orientation as a Key Parameter in Organic Light-Emitting Diodes. *Phys Rev Appl* **8**, 37001 (2017).
7. Mayr, C. & Brütting, W. Control of Molecular Dye Orientation in Organic Luminescent Films by the Glass Transition Temperature of the Host Material. *Chemistry of Materials* **27**, 2759–2762 (2015).
8. Jiang, J., Walters, D. M., Zhou, D. & Ediger, M. D. Substrate temperature controls molecular orientation in two-component vapor-deposited glasses. *Soft Matter* **12**, 3265–3270 (2016).
9. Yokoyama, D. Molecular orientation in small-molecule organic light-emitting diodes. *J Mater Chem* **21**, 19187–19202 (2011).
10. Zhao, L. *et al.* Horizontal molecular orientation in solution-processed organic light-emitting diodes. *Appl Phys Lett* **106**, 063301 (2015).
11. Zhao, G. *et al.* Exceeding 30 % External Quantum Efficiency in Non-doped OLEDs Utilizing Solution Processable TADF Emitters with High Horizontal Dipole Orientation via Anchoring Strategy. *Angewandte Chemie International Edition* **61**, e202212861 (2022).
12. Bagchi, K. & Ediger, M. D. Controlling Structure and Properties of Vapor-Deposited Glasses of Organic Semiconductors: Recent Advances and Challenges. *Journal of Physical Chemistry Letters* **11**, 6935–6945 (2020).
13. Fiori, M. E., Bagchi, K., Toney, M. F. & Ediger, M. D. Surface equilibration mechanism controls the molecular packing of glassy molecular semiconductors at organic interfaces. *Proceedings of the National Academy of Sciences* **118**, e2111988118 (2021).
14. Watanabe, Y., Sasabe, H. & Kido, J. Review of molecular engineering for horizontal molecular orientation in organic light-emitting devices. *Bull Chem Soc Jpn* **92**, 716–728 (2019).
15. Chatterjee, T. & Wong, K.-T. Perspective on Host Materials for Thermally Activated Delayed Fluorescence Organic Light Emitting Diodes. *Adv Opt Mater* **7**, 1800565 (2019).
16. Wong, M. Y. & Zysman-Colman, E. Purely Organic Thermally Activated Delayed Fluorescence Materials for Organic Light-Emitting Diodes. *Advanced Materials* **29**, 1605444 (2017).

17. Degitz, C. *et al.* From Molecule to Device: Prediction and Validation of the Optical Orientation of Iridium Phosphors in Organic Light-Emitting Diodes. *Chemistry of Materials* **35**, 295–303 (2023).
18. Marcato, T. & Shih, C.-J. Molecular Orientation Effects in Organic Light-Emitting Diodes. *Helv Chim Acta* **102**, e1900048 (2019).
19. Sanderson, S. *et al.* Understanding the performance differences between solution and vacuum deposited OLEDs: A computational approach. *J Chem Phys* **156**, 214703 (2022).
20. Olivier, Y., Sancho-Garcia, J.-C., Muccioli, L., D'Avino, G. & Beljonne, D. Computational Design of Thermally Activated Delayed Fluorescence Materials: The Challenges Ahead. *Journal of Physical Chemistry Letters* **9**, 6149–6163 (2018).
21. Tonnelé, C. *et al.* Elucidating the Spatial Arrangement of Emitter Molecules in Organic Light-Emitting Diode Films. *Angewandte Chemie International Edition* **56**, 8402–8406 (2017).
22. Ediger, M. D. Perspective: Highly stable vapor-deposited glasses. *J Chem Phys* **147**, 210901 (2017).
23. Tenopala-Carmona, F. *et al.* Identification of the Key Parameters for Horizontal Transition Dipole Orientation in Fluorescent and TADF Organic Light-Emitting Diodes (dataset). *University of St Andrews Research Portal* (2021) doi:<https://doi.org/10.17630/ae55e842-6db8-4d3b-975c-b1905a0a45f3>.
24. Adhikari, S. & Orrit, M. Progress and perspectives in single-molecule optical spectroscopy. *J Chem Phys* **156**, 160903 (2022).
25. Backlund, M. P., Lew, M. D., Backer, A. S., Sahl, S. J. & Moerner, W. E. The Role of Molecular Dipole Orientation in Single-Molecule Fluorescence Microscopy and Implications for Super-Resolution Imaging. *ChemPhysChem* **15**, 587–599 (2014).
26. Böhmer, M. & Enderlein, J. Orientation imaging of single molecules by wide-field epifluorescence microscopy. *Journal of the Optical Society of America B* **20**, 554–559 (2003).
27. Patra, D., Gregor, I. & Enderlein, J. Image Analysis of Defocused Single-Molecule Images for Three-Dimensional Molecule Orientation Studies. *J Phys Chem A* **108**, 6836–6841 (2004).
28. Deres, A. *et al.* The Origin of Heterogeneity of Polymer Dynamics near the Glass Temperature As Probed by Defocused Imaging. *Macromolecules* **44**, 9703–9709 (2011).
29. Toprak, E. *et al.* Defocused orientation and position imaging (DOPI) of myosin V. *Proc Natl Acad Sci U S A* **103**, 6495–6499 (2006).
30. Lu, J., Mazidi, H., Ding, T., Zhang, O. & Lew, M. D. Single-Molecule 3D Orientation Imaging Reveals Nanoscale Compositional Heterogeneity in Lipid Membranes. *Angewandte Chemie International Edition* **59**, 17572–17579 (2020).
31. Li, P. *et al.* Single-molecule nano-optoelectronics: insights from physics. *Reports on Progress in Physics* **85**, 086401 (2022).
32. Kimura, K. *et al.* Selective triplet exciton formation in a single molecule. *Nature* **570**, 210–213 (2019).

33. Noriega, R. *et al.* Uncovering Single-Molecule Photophysical Heterogeneity of Bright, Thermally Activated Delayed Fluorescence Emitters Dispersed in Glassy Hosts. *J Am Chem Soc* **138**, 13551–13560 (2016).
34. Dedecker, P. *et al.* Defocused Wide-field Imaging Unravels Structural and Temporal Heterogeneity in Complex Systems. *Advanced Materials* **21**, 1079–1090 (2009).
35. Kumar Sharma, D., Hirata, S., Biju, V. & Vacha, M. Stark Effect and Environment-Induced Modulation of Emission in Single Halide Perovskite Nanocrystals. *ACS Nano* **13**, 624–632 (2019).
36. Wöll, D. *et al.* Polymers and single molecule fluorescence spectroscopy, what can we learn? *Chem Soc Rev* **38**, 313–328 (2009).
37. Lupton, J. M. Single-Molecule Spectroscopy for Plastic Electronics: Materials Analysis from the Bottom-Up. *Advanced Materials* **22**, 1689–1721 (2010).
38. Steiner, F., Bange, S., Vogelsang, J. & Lupton, J. M. Spontaneous Fluctuations of Transition Dipole Moment Orientation in OLED Triplet Emitters. *J Phys Chem Lett* **6**, 999–1004 (2015).
39. Vacha, M. & Habuchi, S. Conformation and physics of polymer chains: a single-molecule perspective. *NPG Asia Mater* **2**, 134–142 (2010).
40. Marques, S. R.-M., Selhorst, R. C., Venkataraman, D. & Barnes, M. D. Probing the Evolution of Molecular Packing Underlying HJ-Aggregate Transition in Organic Semiconductors Using Solvent Vapor Annealing. *The Journal of Physical Chemistry C* **123**, 28948–28957 (2019).
41. Lee, D. H. *et al.* Effect of host polarity on efficiency of thermally activated delayed fluorescent and hyperfluorescent organic light emitting devices. *Journal of Industrial and Engineering Chemistry* **117**, 140–148 (2023).
42. Wakelin, S. & Bagshaw, C. R. A prism combination for near isotropic fluorescence excitation by total internal reflection. *J Microsc* **209**, 143–148 (2003).
43. Hutchison, J. A. *et al.* A surface-bound molecule that undergoes optically biased Brownian rotation. *Nat Nanotechnol* **9**, 131–136 (2014).
44. Xu, J. *et al.* Surface structures of poly(methyl methacrylate) films influenced by chain entanglement in the corresponding film-formation solution. *Soft Matter* **10**, 8992–9002 (2014).
45. Zondervan, R., Kulzer, F., Orlinskii, S. B. & Orrit, M. Photoblinking of rhodamine 6G in poly(vinyl alcohol): Radical dark state formed through the triplet. *Journal of Physical Chemistry A* **107**, 6770–6776 (2003).
46. Deschenes, L. A. & Vanden Bout, D. A. Single molecule photobleaching: increasing photon yield and survival time through suppression of two-step photolysis. *Chem Phys Lett* **365**, 387–395 (2002).
47. Bagchi, K. *et al.* Over What Length Scale Does an Inorganic Substrate Perturb the Structure of a Glassy Organic Semiconductor? *ACS Appl Mater Interfaces* **12**, 26717–26726 (2020).
48. Naqvi, B. A. *et al.* What Controls the Orientation of TADF Emitters? *Front Chem* **8**, 750 (2020).
49. Preus, S., Noer, S. L., Hildebrandt, L. L., Gudnason, D. & Birkedal, V. iSMS: single-molecule FRET microscopy software. *Nat Methods* **12**, 593–594 (2015).

50. Imaging of single molecules - Georg-August-Universität Göttingen. <https://www.uni-goettingen.de/en/512319.html>.
51. Archer, E. *et al.* Accurate Efficiency Measurements of Organic Light-Emitting Diodes via Angle-Resolved Spectroscopy. *Adv Opt Mater* **9**, 2000838 (2021).
52. Moon, C.-K., Kim, S.-Y., Lee, J.-H. & Kim, J.-J. Luminescence from oriented emitting dipoles in a birefringent medium. *Opt Express* **23**, A279–A291 (2015).

Supplementary Information

Orientation distributions of vacuum-deposited organic emitters revealed by single-molecule microscopy

Francisco Tenopala-Carmona^{1,2,*}, Dirk Hertel¹, Sabina Hillebrandt¹, Andreas Mischok¹, Arko Graf², Klaus Meerholz¹, Malte C. Gather^{1,2,*}

3. Humboldt Centre for Nano- and Biophotonics and Institute of Physical Chemistry, Department of Chemistry, University of Cologne, Greinstr. 4-6, 50939 Köln, Germany.
4. Organic Semiconductor Centre, SUPA School of Physics and Astronomy, University of St Andrews, St Andrews, KY16 9SS, UK.

*Email: Malte.Gather@uni-koeln.de, F.TenopalaCarmona@uni-koeln.de

S1. Hypothetical orientation distributions

An ensemble of dipoles that follows an isotropic distribution can be represented by a uniform distribution of points over the unit sphere. This distribution of points scales proportionally to the surface area as a function of the polar angle θ , i.e., $P(\theta) \propto \sin(\theta)$. This can be seen in **Figure S1a**, which shows an array of 2000 random points uniformly distributed over the unit sphere. By contrast, **Figure S1b** shows an array of 2000 points normally distributed over the same sphere, with a mean value of 31.23° and a standard deviation of 11.46° . The histograms shown in **Figure 1a** of the main text follow the same distributions, but contain data from 100,000 points. All hypothetical distributions were generated using the software Matlab using the functions *rand* for uniformly distributed points or *normrnd* for normally distributed points).

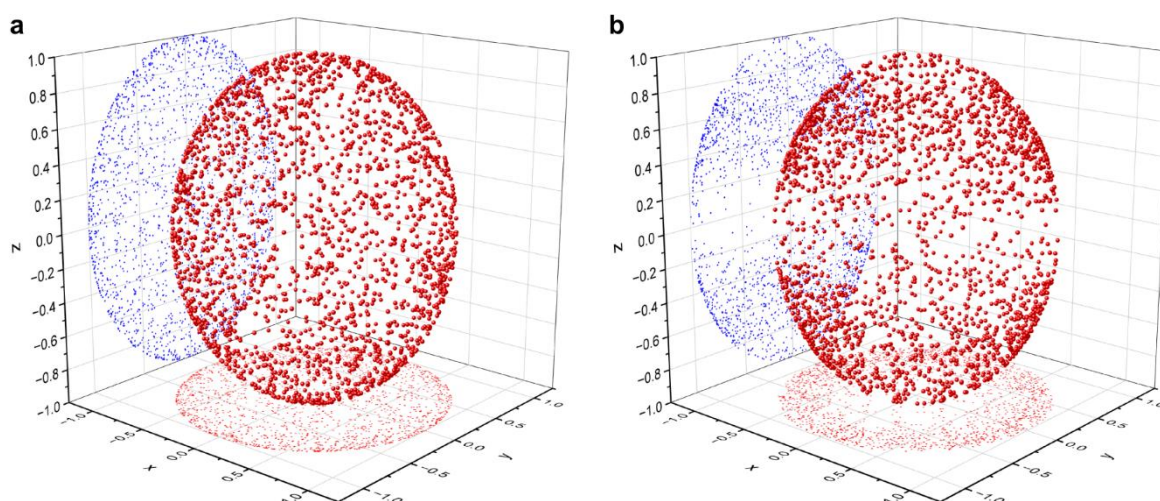


Figure S5. Graphical representation of orientation distributions. a, isotropic and **b**, non-isotropic distributions. Both have the same anisotropy factor $a = \langle \cos^2\theta \rangle = 0.33$.

S2. Obtaining orientation distributions from single-molecule defocused orientation and position imaging data.

First, we used optical models from the Matlab package QDControl, which follows the theory described by Böhmer and Enderlein in ¹, to generate a library of r defocused patterns:

$$P^{(r)} = P^{(r)}(x, y, z, \theta, \phi, dz, d, n_{\text{host}}, n_{\text{substrate}}, NA, M, \lambda),$$

where x , y , and z are the Cartesian coordinates of the transition dipole within the film, θ and ϕ are the polar and azimuthal orientation angles, dz is the out-of-focus distance, d is the thickness of the film, n_{host} and $n_{\text{substrate}}$ are the refractive indices of the film and the substrate, respectively, NA is the numerical aperture of the microscope objective (1.45), M is the total magnification of the system (280 \times), and λ is the wavelength of the emitted light (520 nm due to the narrow band-pass filter in the imaging path). d , n_{host} and $n_{\text{substrate}}$ were obtained from ellipsometry measurements and dz was controlled using the Perfect Focus System of the microscope, which allows accurate control of the position of the objective with respect to the substrate. For the experiments done in PMMA, z , θ , ϕ were set to vary in the pattern library. For thermally evaporated samples, z was fixed at the known position of the molecules and θ , ϕ were varied.

Next, we followed the algorithm introduced by Patra and Enderlein² to calculate the minimum error for each pattern from the library centred at each pixel (m, n) of the experimental image:²

$$e_{mn}^{(r)} = \sum_{j,k} s_{jk} \left(x_{m+j, n+k} - c_{mn}^{(r)} p_{jk}^{(r)} - d_{mn}^{(r)} b_{jk} \right)^2,$$

where j and k denote the pixels of a subsection of the image centred at pixel m, n , s is a circular mask consisting of values 1 and 0 only, c is a constant that accounts for the brightness of each pattern, b is a uniform normalised background value, and d is a scaling factor for the background. From this calculation, the minimum value of $e_{mn}^{(r)}$ at each pixel m, n , \tilde{e}_{mn} , is identified, and thereby the best-fitted pattern $P^{(r)}$ for that pixel is selected. Then, these values are used to generate a map of the inverse minimum error for each pixel weighted by the brightness of the corresponding pattern, $L_{mn} = \tilde{c}_{mn} / \sqrt{\tilde{e}_{mn}}$. Thresholding of this map leads to the identification of the position of the molecules in the image.

However, as pointed out by Patra and Enderlein, due to the symmetry of the defocused patterns for wide polar angles (see **Figure 1c** of the main text), single defocused patterns lying close to the horizontal can be misidentified as two independent patterns with values of θ close to the vertical. Therefore, we implemented an additional segmentation algorithm described below and illustrated in **Figure S2**.

1. Thresholding of the inverse error map L_{mn} with low threshold values (0.5).
2. Calculation of a distance-transformed map of the pixels above threshold.
3. Filtering of the distance-transformed map using a 2D median filter.
4. Segmentation using a Watershed transform.

From that segmentation, each cluster of pixels above threshold was treated as a region belonging to the same identified molecule. Then, the maximum value of L_{mn} was identified, its corresponding pixel was selected as the best fitted position for that molecule, and the corresponding values of $P^{(r)}$, \tilde{c}_{mn} , and $d_{mn}^{(r)}$ were selected as its best fitted pattern, brightness, and background, respectively. Finally, a threshold value for L_{mn} depending on the signal-to-

noise ratio of the specific measurement was selected and patterns below that threshold were discarded. This threshold was set to 1.0, 0.7, and 1.8 for the experiments in PMMA, on bare glass, and in mCP, respectively.

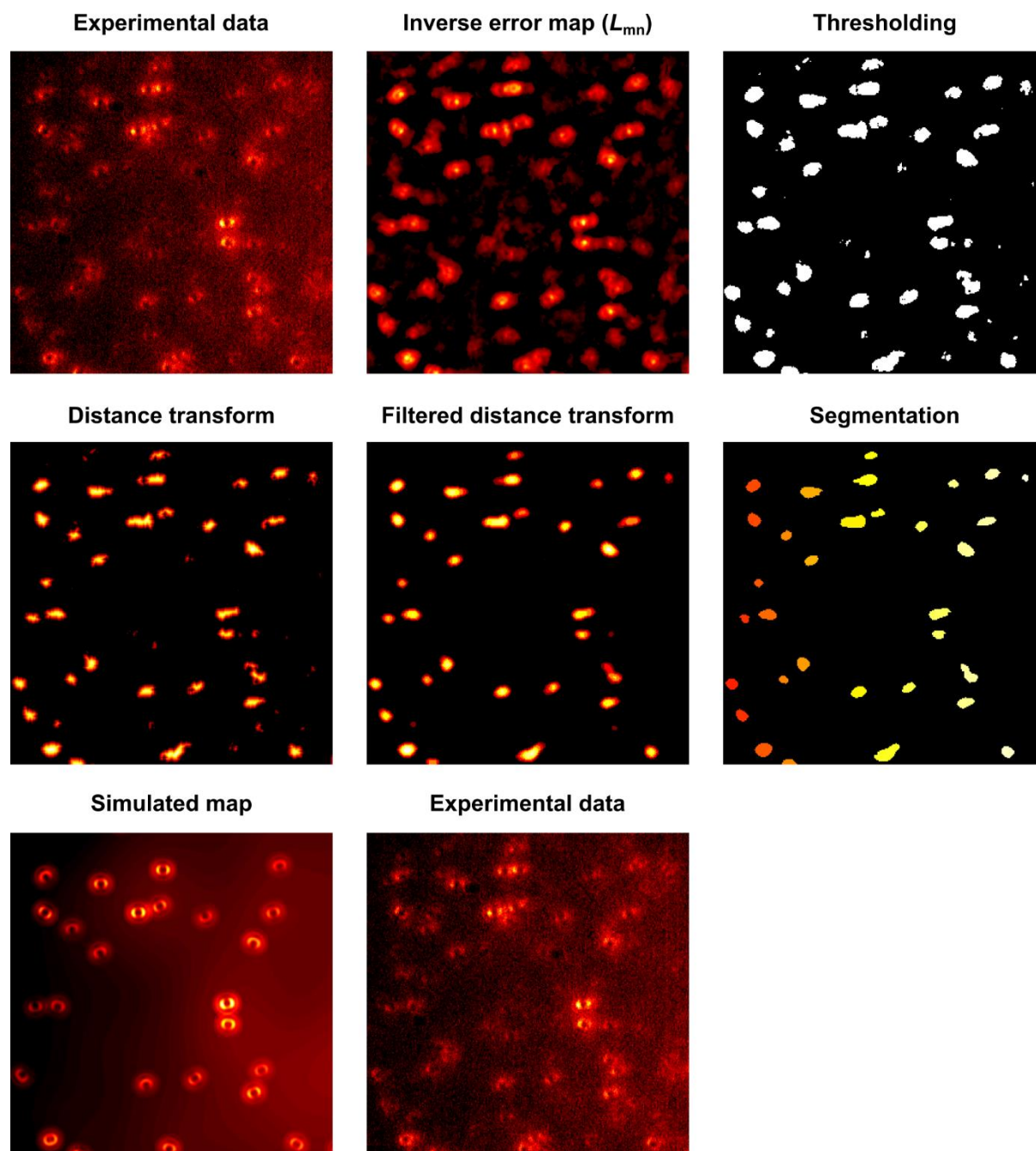
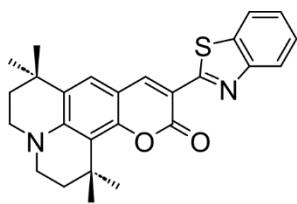
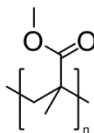


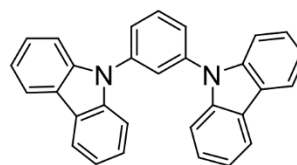
Figure S6. Graphical description of the segmentation algorithm used for DOPI data analysis. The experimental data is shown twice for direct comparison with the simulated and inverse-error maps.



C545T



PMMA



mCP

Figure S7. Structure of the materials used in this work.

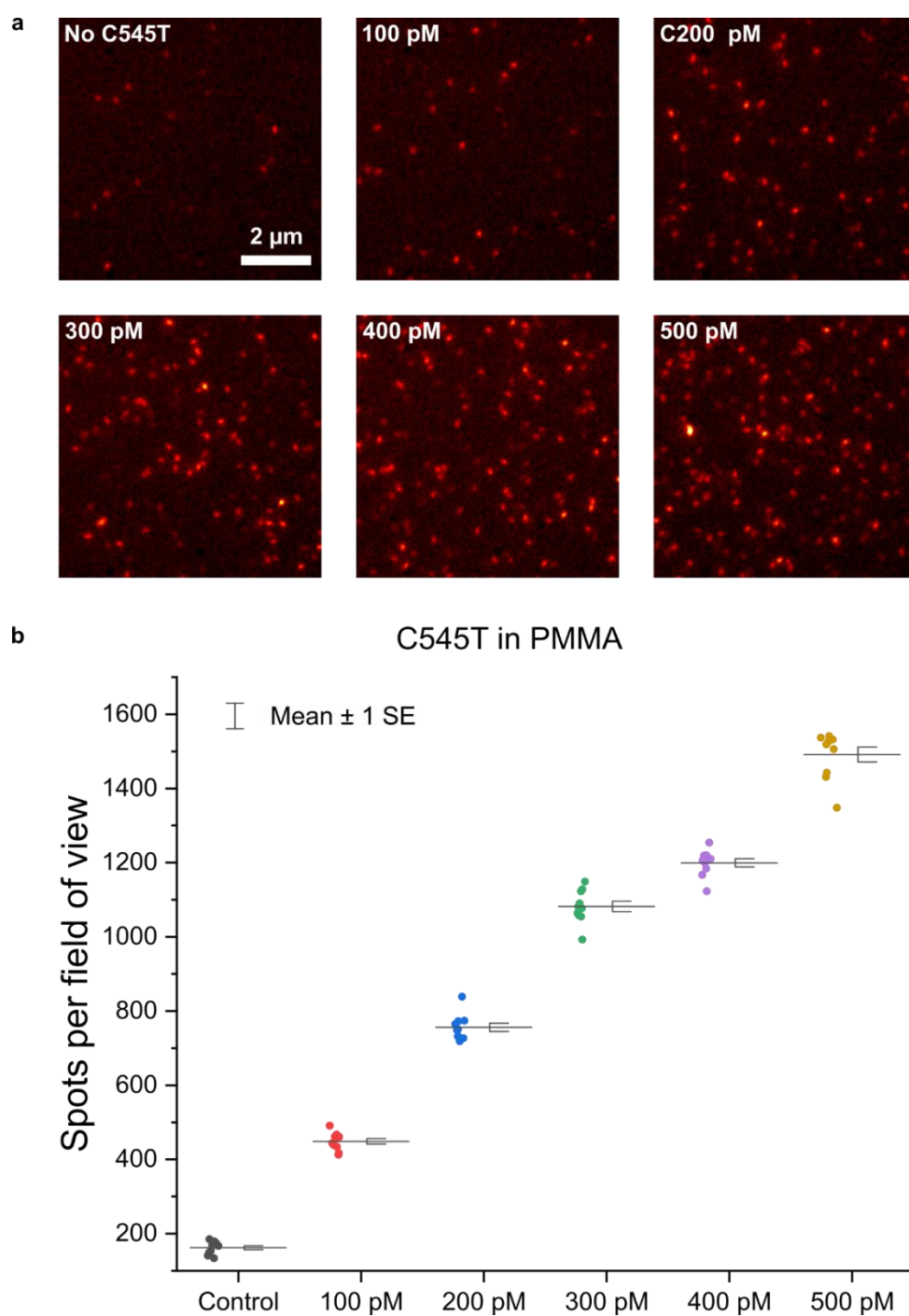


Figure S4. Measurement of number of molecules per field of view in samples for single-molecule microscopy. a, Fluorescence microscopy images of spin-coated samples of C545T in PMMA. The label indicates the concentration of C545T in the coated dilution. **b,** Number of molecules per field of view found in the corresponding solution-processed samples. The control sample is made of PMMA only (no C545T).

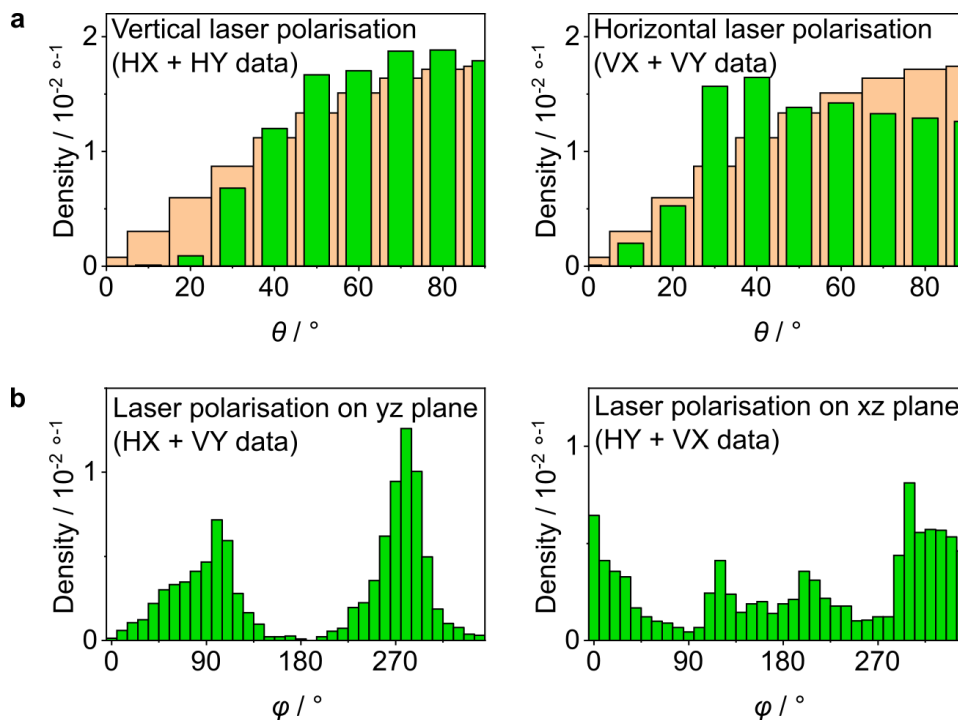


Figure S5. Correlation of the measured TDM orientation angles and the different polarised excitation conditions. **a**, Distribution of polar angles for the combined datasets measured using HX + HY (horizontal) excitation and VX + VY (vertical) excitation. The distribution is shifted towards smaller or larger angles for vertical and horizontal excitation, respectively. **b**, Distribution of azimuthal angles for the combined datasets measured using HX + VY (excitation parallel to the yz plane) and HY + VX (excitation parallel to the xz plane), respectively. The peaks in the distributions are located at complementary positions.

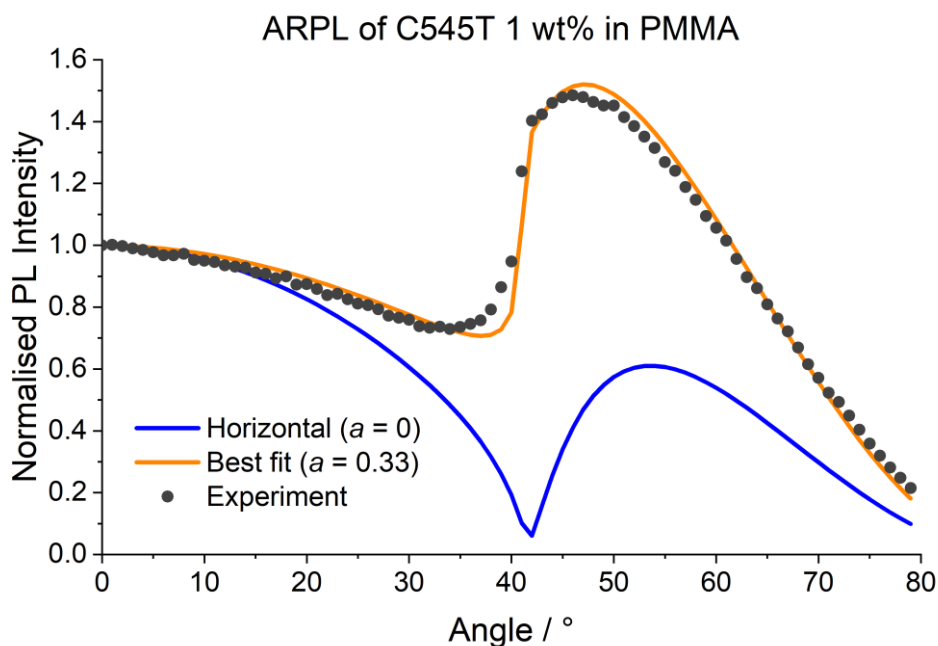


Figure S6. Angle-resolved photoluminescence measurements of spin-coated C545T dispersed at 1 wt% in PMMA.

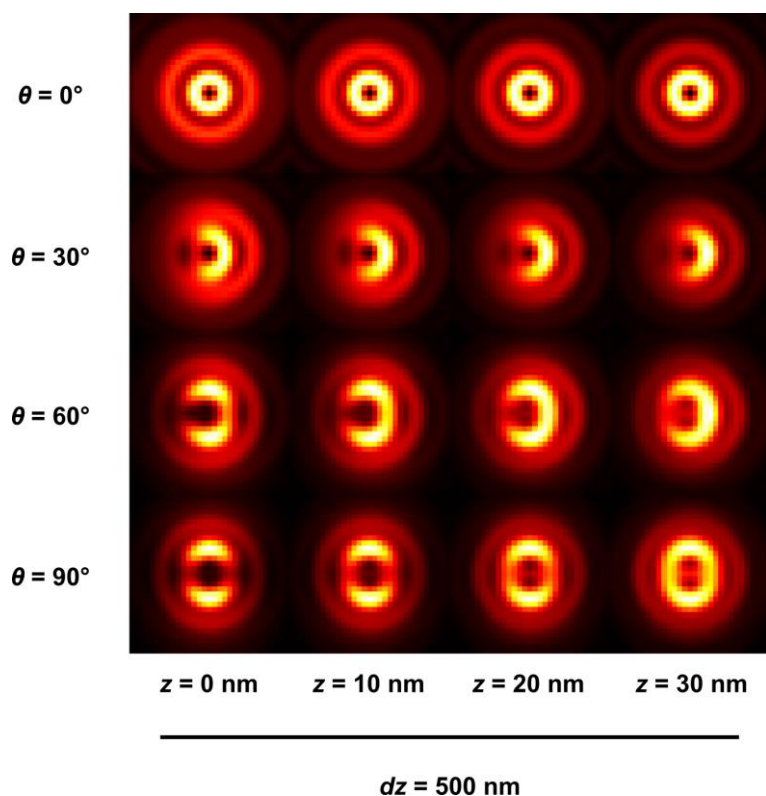


Figure S7. Optical simulations of defocused orientation patterns as a function of the polar angle TDM of the molecule and its z -position within the film. Defocussing dz was 500 nm for all simulations.

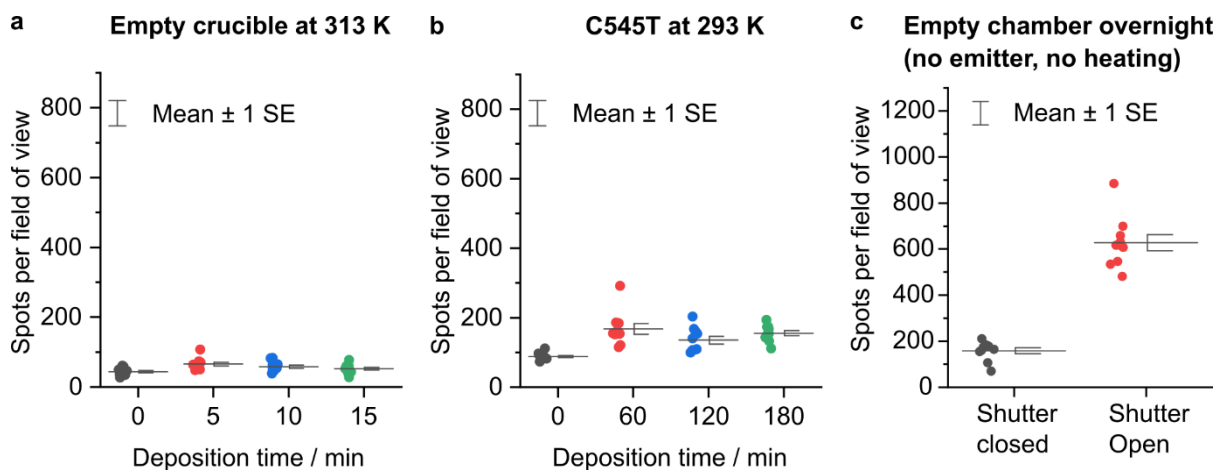


Figure S8. Control tests for thermally evaporated samples of C545T on bare glass. a, Quantification of the base level of fluorescent impurities by mapping the number of emissive spots per field of view ($\sim 40 \times 40 \mu\text{m}^2$) in a control run with substrates exposed to **a**, a heated but empty crucible, **b**, a crucible with C545T with no active heating, and **c**, the evaporation chamber in high vacuum overnight with no crucibles nor active heating. There is no correlation between the number of spots and the exposure time for periods within the duration of our emitter deposition processes for the samples used in single-molecule microscopy measurements. Furthermore, the impurity level in this range is well below the target

concentration in **Figure 3b** of the main text, and it only becomes more significant for long exposure times (panel c).

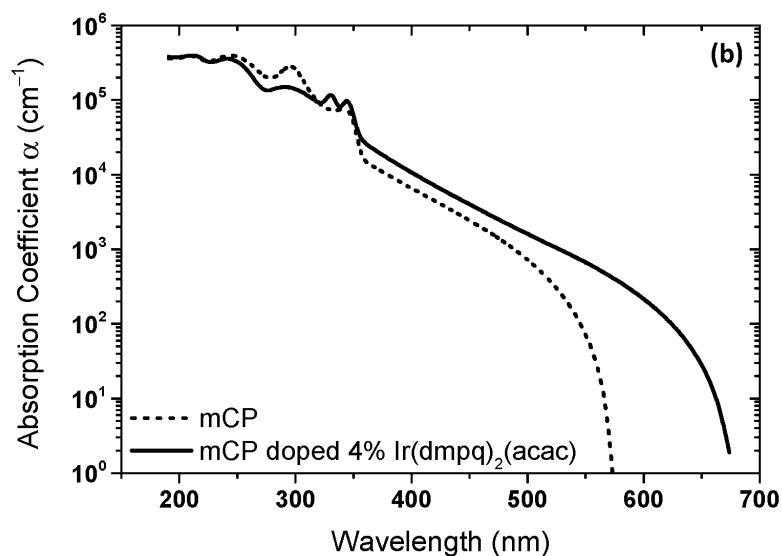


Figure S9. Absorption spectrum of mCP with absorption coefficient shown on a logarithmic scale. Reproduced from reference ³ under the Creative Commons Attribution (CC BY) license (<https://creativecommons.org/licenses/by/4.0/>).

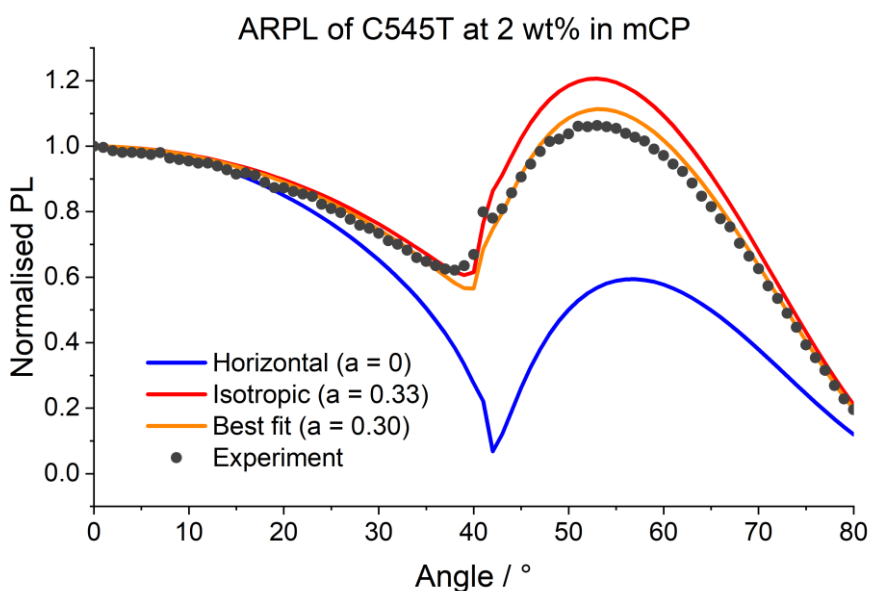


Figure S10. Angle-resolved photoluminescence measurements of C545T dispersed at 2 wt% in mCP.

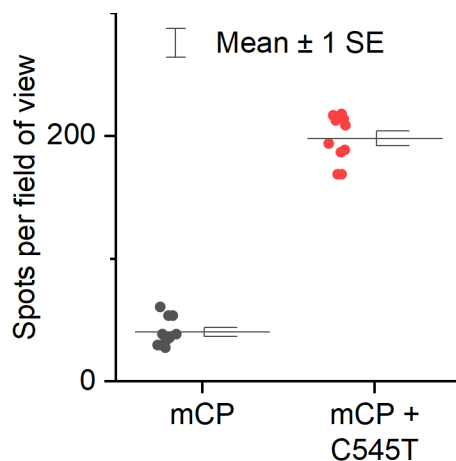


Figure S11. Number of emissive molecules per field of view found in thermally evaporated samples for single-molecule microscopy. The control sample (mCP) was covered during the deposition of the emitter layer using adjustable shutters and consists only of a 40 nm layer of purified host material. The “mCP + C545T” sample was fabricated as depicted in **Fig. 4d** of the main text.

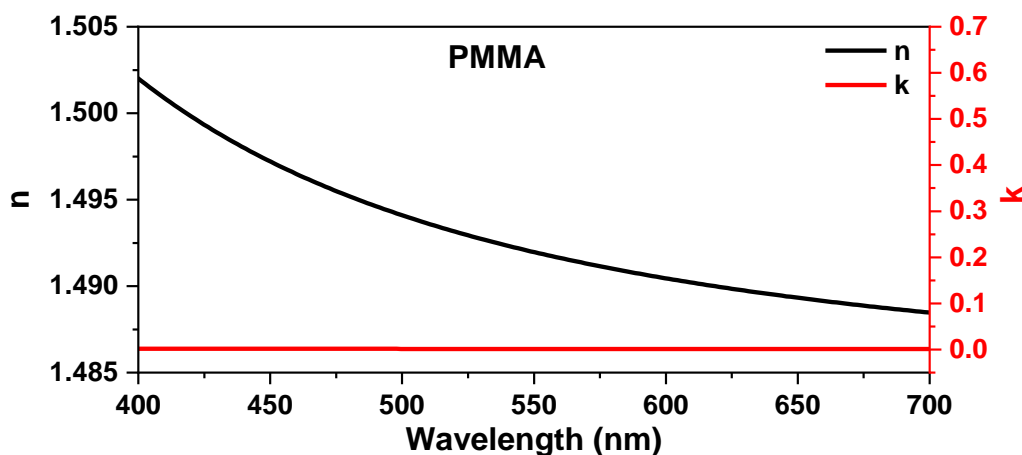


Figure S12. Optical constants of PMMA. No significant improvement in fit quality over what is shown here was obtained when fitting the ellipsometry data to a birefringent model of the optical constants.

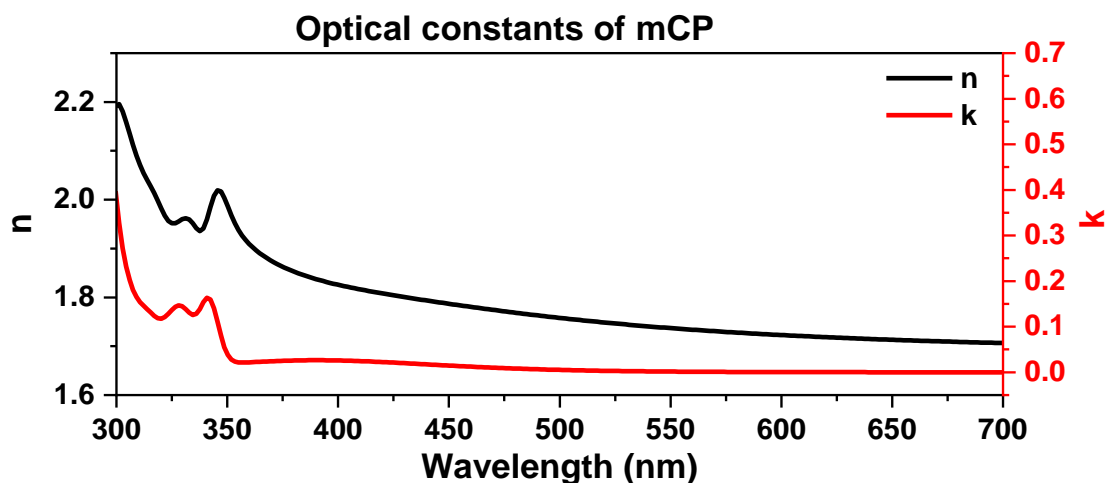


Figure S13. Optical constants of mCP. No significant improvement in fit quality over what is shown here was obtained when fitting the ellipsometry data to a birefringent model of the optical constants.

References

1. Böhmer, M. & Enderlein, J. Orientation imaging of single molecules by wide-field epifluorescence microscopy. *Journal of the Optical Society of America B* **20**, 554–559 (2003).
2. Patra, D., Gregor, I. & Enderlein, J. Image Analysis of Defocused Single-Molecule Images for Three-Dimensional Molecule Orientation Studies. *J Phys Chem A* **108**, 6836–6841 (2004).
3. Tselekidou, D., Panagiotidis, L., Papadopoulos, K., Kyriazopoulos, V. & Gioti, M. A Comparative Study of Ir(dmpq)₂(acac) Doped CBP, mCP, TAPC and TCTA for Phosphorescent OLEDs. *Photonics* **9**, 800 (2022).